

# Advanced Physics Laboratory

Study of Solid State Surfaces using a Scanning Tunnelling  
Microscope

Name: Nicolò De Masi, Manthan Chattopadhyay

Experiment Date: 25.06.2024



## **Abstract**

This report presents investigation of sample surfaces conducted using the Nanosurf Naio STM and Gwyddion software. A calibration grid with aluminum bumps on silicon was scanned to evaluate grid spacing and thermal drift during scan time. A Gold (111) sample's surface morphology was examined to identify grain and mound formation due to Ehrlich-Schwoebel barrier. Histogram analyses of 36 InAs quantum dots on GaAs substrates were performed to obtain mean height and volume. Graphite surface morphology was optimized by adjusting PID values, leading to the determination of lattice constants and atomic distances. Lastly, a TaS<sub>2</sub> surface was studied to observe CDW states and determine the lattice constants.

# Contents

<b>1 Theoretical Background</b>	<b>4</b>
1.1 The Scanning-Tunneling-Microscope . . . . .	4
1.1.1 Quantum Tunneling . . . . .	4
1.1.2 Piezoelectric effect . . . . .	7
1.1.3 Proportional-Integral-Derivative (PID) Controller . . . . .	9
1.1.4 Operating Modes . . . . .	10
1.2 Investigation of Materials . . . . .	10
1.2.1 Periodicity of Crystals . . . . .	11
1.2.2 Surface Grains in Gold . . . . .	11
1.2.3 Quantum dots . . . . .	12
1.2.4 Graphite . . . . .	12
1.2.5 Tantalum(IV) Sulfide . . . . .	13
<b>2 Experimental Setup</b>	<b>14</b>
2.1 easyScan Operational Principle . . . . .	14
2.2 Tip & Sample Handling . . . . .	15
<b>3 Results &amp; Discussion</b>	<b>16</b>
3.1 Measurements of the Calibration Grid . . . . .	16
3.2 Gold (111) Sample . . . . .	18
3.3 InAs Quantum Dots on a GaAs Surface . . . . .	19
3.4 Graphite Surface Morphology . . . . .	21
3.5 Charge Density Wave State of TaS <sub>2</sub> . . . . .	23
<b>4 Conclusion &amp; Outlook</b>	<b>27</b>
<b>A Crystal Systems and their d-spacing</b>	<b>31</b>

# 1 Theoretical Background

Scanning Tunneling Microscopy (STM) has revolutionized the fields of electronics and optoelectronics by enabling the exploration of nanometer-scale structures and further miniaturizing electronics from the micrometer to the nanometer scale. This also led to the synthesis of quantum dots, a semiconductor device with atomic dimensions ( $< 100 \text{ nm}$ ).

Due to the limited resolving power of visible light, we require measurement techniques beyond the capabilities of traditional optical microscopy. To overcome this limitation, scanning processes like Scanning Electron Microscopy (SEM) and STM were developed. SEM uses a focused beam of electrons to produce atomic-scale images, while STM offers direct imaging of surface topography with atomic resolution without damaging the samples.

STM was developed by Gerd Binnig and Heinrich Rohrer at IBM's Zurich Research Laboratory in the early 1980s, a breakthrough for which they received the Nobel Prize in Physics in 1986 [1]. It has since become a standard tool for surface analysis, capable of examining both inorganic crystals and organic substances. Typically operated in ultrahigh vacuum to prevent surface oxidation, the STM used in our experiment, the *easyScan* model, is designed for practical training and operates in air.

## 1.1 The Scanning-Tunneling-Microscope

The STM consists of a very thin metallic tip positioned within less than 1 nm of a conducting or semiconducting sample using piezo positioning elements. When a voltage of 0.1 to 1 V is applied between the tip and the sample, a current flows across the gap due to quantum tunneling. This tunneling current is dependent on both the tip-sample distance and the surface structure. During scanning, the tip moves line by line over the sample, with piezoelements adjusting the distance to maintain a constant tunneling current. The recorded distances are mapped according to their positions on the surface, creating an "image of constant tunnel current" that reflects both the geometrical surface structure and electron probability distribution. High resolution in STM requires minimal scanning step lengths, achieved through piezoelements based on the inverse piezoelectric effect as explained in Section 1.1.2. The STM employs three piezoelements: two scan in the x-y plane parallel to the surface, while the third maintains a constant tunnel current in the z direction through a control loop (constant current mode). For very flat surfaces however, the tip can be made to scan at a fixed distance and measure tunneling current as a function of x-y coordinates (constant distance mode). For the *easyScan* microscope, the minimum step length is 0.015 nm in the z direction and 0.1 nm in the x and y directions.

### 1.1.1 Quantum Tunneling

The manifestation of quantum tunneling was first interpreted by Oscar Rice upon studying the rotationally induced dissociation of a diatomic molecule from an excited state, observed through the broadening of infrared spectral lines [4]. While being a National Research Fellow in Leipzig, Rice consulted Heisenberg, Felix Bloch, and Hendrik Kramers in order to treat the theory of this breakup.

Consider an arbitrary potential  $V(x)$ :

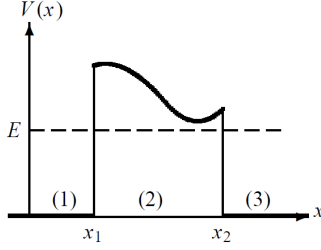


Figure 1: An arbitrary potential barrier with classically allowed zones (1) and (3) [5]

with a particle of momentum  $p_0 = \sqrt{2mE}$  incident from left. For (1) and (3),

$$\begin{aligned}\psi_1(x) &= \psi_{\text{incident}}(x) + \psi_{\text{reflected}}(x) = Ae^{ip_0x/\hbar} + Be^{-ip_0x/\hbar} \\ \psi_3(x) &= \psi_{\text{transmitted}}(x) = Ee^{ip_0x/\hbar}\end{aligned}\quad (1)$$

Since  $E < V_{\max}$  in (2), we apply the WKB approximation such that

$$\psi_2(x) = \frac{C}{\sqrt{|p(x)|}} \exp \left[ -\frac{1}{\hbar} \int_{x_1}^x |p(x')| dx' \right] + \frac{D}{\sqrt{|p(x)|}} \exp \left[ \frac{1}{\hbar} \int_{x_1}^x |p(x')| dx' \right] \quad (2)$$

where  $p(x) = i\sqrt{2m(V(x) - E)}$ . The second term with  $D$  increases exponentially as the barrier widens is therefore unphysical. Considering a barrier wide enough that permits the approximation  $D \simeq 0$ ,  $\psi_2(x)$  becomes

$$\psi_2(x) = \frac{C}{\sqrt{|p(x)|}} \exp \left[ -\frac{1}{\hbar} \int_{x_1}^x |p(x')| dx' \right] \quad (3)$$

One finds the probability corresponding to the particle's passage through the barrier via the transmission coefficient

$$T = \frac{v_{\text{trans}} |\psi_{\text{trans}}(x)|^2}{v_{\text{inc}} |\psi_{\text{inc}}(x)|^2} = \frac{|E|^2}{|A|^2} \quad (4)$$

Applying continuity of wave function and its derivative at the boundaries  $x_1$  and  $x_2$ , we eventually get an approximate value of T as

$$T \sim e^{-2\gamma}, \quad \gamma = \frac{1}{\hbar} \int_{x_1}^{x_2} \sqrt{2m(V(x) - E)} dx \quad (5)$$

For a constant potential barrier of the sort,

$$V(x) = \begin{cases} 0 & x < x_1 \\ V_B & x_1 \leq x \leq x_2 \\ 0 & x > x_2 \end{cases} \quad (6)$$

the transmission coefficient becomes:

$$T = \left[ 1 + \frac{1}{4} \left[ \frac{1}{\frac{E}{V_B} \left( 1 - \frac{E}{V_B} \right)} \right] \sinh^2 \left[ \frac{s}{\hbar} \sqrt{2m(V_B - E)} \right] \right]^{-1} \quad (7)$$

for  $E < V_B$ . In the case of a high barrier with  $(x_2 - x_1)p(x) \gg 1$  for  $x \in (2)$ , it holds that:

$$\sinh^2 \approx \frac{1}{4} \exp \left\{ \frac{2}{\hbar} \sqrt{2m(V_B - E)}(x_2 - x_1) \right\} \quad (8)$$

Equation (7) thus becomes,

$$T = \frac{16E(V_B - E)}{V_B^2} \exp \left\{ \frac{-2(x_2 - x_1)}{\hbar} \sqrt{2m(V_B - E)} \right\} \quad (9)$$

where  $E = eU \ll V_B$  and which albeit decaying exponentially with barrier thickness, is finite.

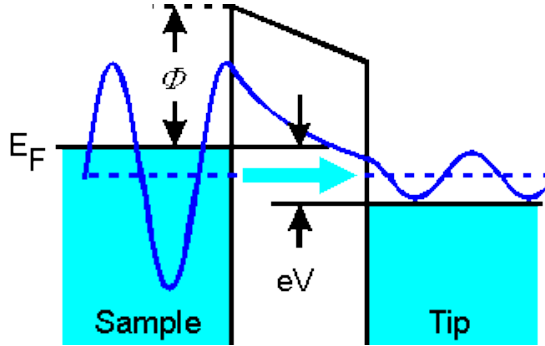


Figure 2: Illustration of the Fermi levels for a metallic surface and tip with the tip biased positive relative to the surface. At a positive tunneling voltage ( $eV$ ) applied to the tip, the electrons from the occupied states in the valence band of the sample are caused to travel through the barrier to the unoccupied states of the tip. [6]

In our case, the sample and tip have different work functions  $\Phi$  and Fermi levels  $E_F$ . This creates an inclined  $V_B$  as shown in Figure 2. Hence, we take an average barrier height  $\Phi_m$ . In the case that tip-sample distance and applied voltage is small ( $eU \ll \Phi_m$ ), the tunnel current becomes [7]:

$$I(x_1, x_2, U) = \frac{eU\hbar}{2m_e} N(E_F) G \exp \left\{ -A(x_2 - x_1) \sqrt{\Phi_m} \right\} \quad (10)$$

where  $A = 10.25 \text{ eV}^{0.5} \cdot \text{nm}^{-1}$ ,  $N(E_F)$  the density of states at the Fermi level of the negative electrode, and  $G$  a factor of tip geometry. This exponential decrease of tunneling current with tip-sample distance has been found for both equal and different tip-sample materials, as well as for high and low voltages. The linear dependence between  $I$  and  $U$  is depicted in Figure 3.

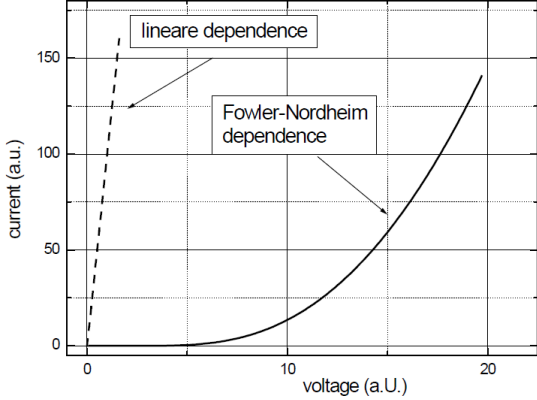


Figure 3: Linear I-U dependence for small tip-sample distance and voltage (dashed). Quadratic I-U dependence for large tip-sample distance and voltage (solid) [7]

In the case of  $eU \gg \Phi_m$  and large tip-sample distance, tunnel current becomes the Fowler-Nordheim equation:

$$I(U) \propto \frac{U^2}{\Phi_m} \exp\left\{-\frac{c_1 \Phi^3/2}{U}\right\} \quad (11)$$

where  $c_1$  is a constant and the dependence of  $I$  on tip-sample distance is lifted.

### 1.1.2 Piezoelectric effect

Given we detect a tunnel current, it is now imperative to move the tip with atomic precision which requires an accuracy of about  $10^{-11}$  m for all three spatial coordinates. This is achieved by the so-called inverse piezoelectric effect, the direct version of which was first realized by Pierre Curie and Jacques Curie in 1880. An electric charge proportional to mechanical stress was created (direct piezo effect) in single crystals such as quartz ( $\text{SiO}_2$ ). The converse, a geometric strain proportional to an applied voltage was also soon realized [11].

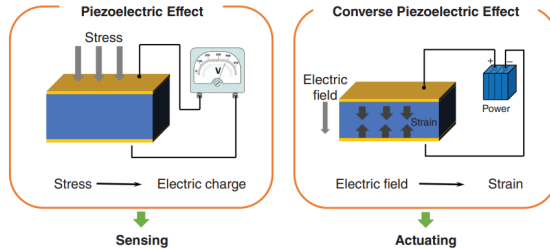


Figure 4: The direct piezoelectric effect provides an electric charge upon application of a mechanical stress, whereas the converse piezoelectric effect describes the situation where strain develops under an applied electric field. [11]

For certain crystals, mechanical deformation causes a shift in atomic centers of charge, leading to crystal polarization, generation of surface charges and

therefore measurable voltages. This effect is observed in crystals with a polar axis, lacking a center of inversion, and cannot be replicated by rotating around the polar axis. Quartz is the most well-known piezoelectric crystal, but many other crystals with varying piezoelectric coefficients also exist. In particular, ceramic piezoelements have become widely used in various applications.

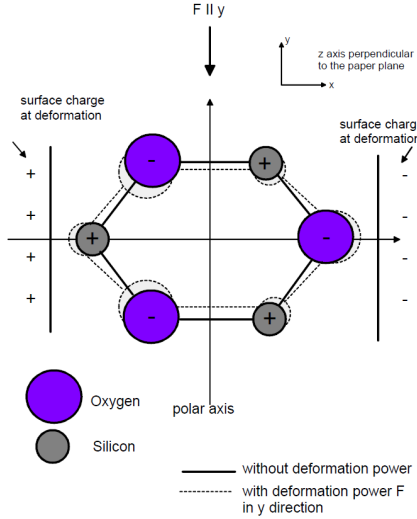


Figure 5: Piezoeffect in  $\text{SiO}_2$  crystal due to spatial deformation [7]

If one applies a force  $\mathbf{F} = F\hat{\mathbf{y}}$  the separation of charges along the x-axis induces a polarization and surface charges at the deformation. Quartz belongs to trigonal crystal system and space group  $P3_121$  with three-fold rotational symmetry along the z-axis. Hence, a force  $\mathbf{F} = F\hat{\mathbf{x}}$  and deformation along y-axis does not induce polarization due to mirror symmetry along x-axis. The applied force and piezocharge  $Q$  are proportional as

$$Q = d \cdot F \quad (12)$$

where  $d$  is the piezoelectric constant of the material. The generated charge  $Q$  creates a voltage  $V$  which is proportional to the charge via the capacitance of the material. If we consider the stress  $\sigma = F/A$ , equation (12) changes to

$$\frac{Q}{A} \equiv P = d\sigma \quad (13)$$

where  $P$  is the induced polarization. The inverse piezoeffect can be exhibited if a voltage is applied to the crystal that forces a deformation such that

$$\Delta l = d \cdot V \quad (14)$$

where  $\Delta l$  is the change in length. In STM, voltage is applied to piezoelectric actuators which expand or contract thus moving the tip closer or further from the surface. A detailed discussion of experimental setup is performed in Section 2.

### 1.1.3 Proportional-Integral-Derivative (PID) Controller

A PID controller is a control loop feedback mechanism widely used in industrial control systems. It continuously calculates an error value as the difference between a desired setpoint and a measured process variable, and applies a correction based on proportional, integral, and derivative terms. In STM, maintaining a constant tunneling current is critical for obtaining accurate images of the surface. This is achieved by precisely controlling the distance between the STM tip and the sample surface. A PID controller is employed to manage this control loop effectively.

Upon measurement of the tunneling current, the control ensures if the current is too low (too high), the distance to the sample is reduced (increased).

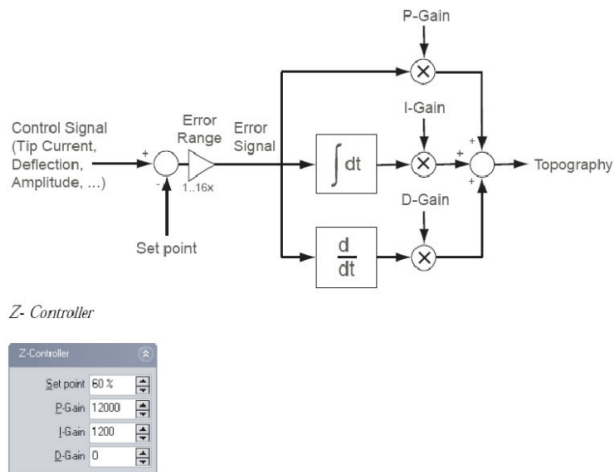


Figure 6: Schematic of PID controller in the STM. The corresponding control parameters can be set in the NaioSTM control software [12]

For small deviations  $E(t)$  from setpoint  $S$ , for a measured current signal  $I(t)$ , one can change the distance proportionally such that an error signal  $E(t) = I(t) - S$  is obtained resulting in manipulated variable  $Y(t) = gE(t)$  where  $g$  is a proportionality constant (or gain). However, a proportional control leads to a permanent control error (eg. offshoot in heating systems).

This error can be eliminated by transforming constant value  $E(t)$  into a time-increasing manipulated variable until the setpoint is reached [13]. This is done by integrating  $E(t)$  over a period  $T_I$  and adding it to the manipulated variable such that

$$Y(t) = gE(t) + \frac{h}{T_I} \int_{t-T_I}^t E(\tau)d\tau \quad (15)$$

For rapidly changing currents, the tendency of the error signal should be evaluated. A fast variation in  $I(t)$  leads to a fast change of  $Y(t)$  even before the proportional part intervenes in the control due to a large deviation. This can be achieved by introducing a differential component such that:

$$Y(t) = gE(t) + \frac{h}{T_I} \int_{t-T_I}^t E(\tau)d\tau + jT_D \frac{dE(t)}{dt} \quad (16)$$

A setback of this is that it amplifies external perturbations and the control loop tries to compensate for them.

#### 1.1.4 Operating Modes

During imaging, one can take an image of the z-signal or the tunnel current  $I$ . The information content however differs between two primary modes:

- Constant Current Mode: For a fixed tunnel voltage, a setpoint of the tunnel current is set which is achieved by varying tip-sample distance. This enables the tip to conform to uneven topographies. In practice the tunnel current is seldom constant, with deviations hinting at quality of control as depicted in Figure 7:

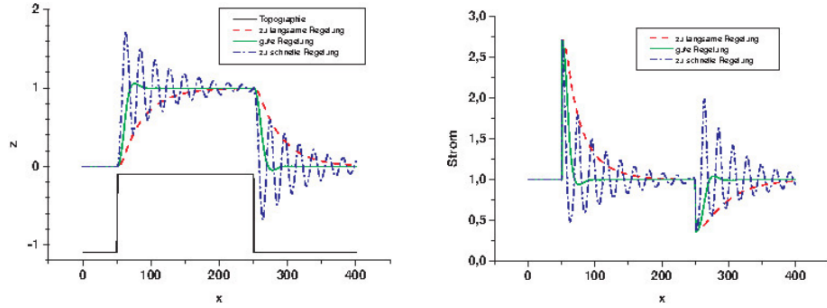


Figure 7: Simulation of  $z$  (left) and current (right) signal in constant current mode. The tip moves from left to right. [13]

The ideal curve would present a constant distance  $z$  to the topography (black), approximated satisfactorily by the green curve. An overshoot occurs if the tip is too fast (blue), whereas an initial delay is seen in the case the tip moves slow. Most of our report employs the constant current mode.

- Constant height mode: This mode is used specifically for flat surfaces. The tip is moved in plane parallel to the sample surface with minimal feedback pertaining to sample surface skewness. The average inclination of the surface is compensated with a very slowly adjusted control loop. A higher scanning speed can be exploited here to negate thermal drift effects throughout the scan.

## 1.2 Investigation of Materials

STM allows us to obtain high-resolution images of a wide variety of sample materials. This gives information about impurities and structure of the sample, as well as surface morphology with respect to the fabrication procedure. Understanding the crystal lattice structure is crucial to interpreting these images accurately.

### 1.2.1 Periodicity of Crystals

The Scanning Tunneling Microscope relies on the periodicity of crystals for proper functioning. Crystals are characterized by a highly ordered microscopic structure, with molecules forming a crystal lattice that extends in all directions.

The building block of a crystal structure is the unit cell, defined as the smallest group of atoms which maintains the overall symmetry of a crystal, and from which the entire lattice can be spanned. It is characterized by three vectors  $\mathbf{a}, \mathbf{b}, \mathbf{c}$ , as well as the angles  $\alpha, \beta, \gamma$  between them. Different values of these parameters result in 7 total crystal systems, as illustrated in Appendix A.

### 1.2.2 Surface Grains in Gold

Gold is a face-centered cubic (FCC) crystal, i.e. with a gold atom on each corner and on the center of each face of the unit cell. At room temperature,  $a = b = c = 4.08 \text{ \AA}$ .

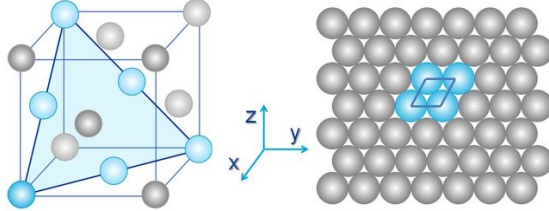


Figure 8: Unit cell of a face-centered cubic crystal (left) showing the position of the (111) plane, and atomic structure of the corresponding (111) surface (right) [3]

The crystal plane most commonly observed is given by the (111) arrangement, which cuts the diagonal of the base of the crystal cells (Fig. 8(left)). This leads to a hexagonal arrangement of atoms (Fig. 8(right)), for an overall very densely packed structure, which gives gold its excellent electrical conductivity and chemical inertness. This dense, homogeneous distribution, however, make it harder to obtain good images of the crystal arrangement of gold.

The STM measurements with gold samples instead focus on the larger structural elements of surface grains, an important type of defects controlling the properties of materials.

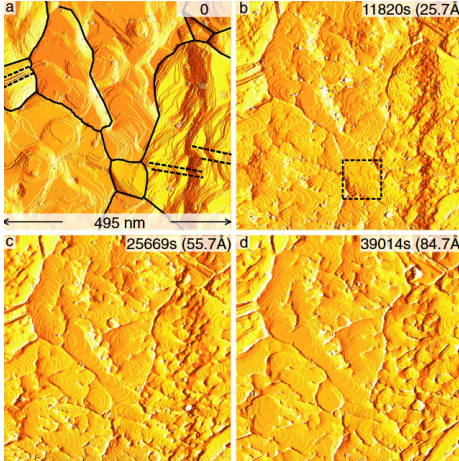


Figure 9: STM images taken during the deposition of a poly-crystalline Au film at 293 K. In (a), black lines underline the grain boundaries and dashed lines twin boundaries [9].

Surface grains in poly-crystalline materials such as gold, refer to distinct regions on the surface where atoms clump up in differently oriented structure, each with its own repeating pattern called grains. Each grain can be observed as its own lattice, with a different orientation, and boundaries in-between them are referred to as grain boundaries. Their presence is motivated by the generally anisotropic surface energy - due to atoms at the surface having some of their neighbours missing, and thus no cohesive bonds on that side, resulting in particular crystal shapes with different orientations explained by a Wulff plot construction. [15]

The development of preferred orientation or texture is of considerable importance in industrial processes as well as in giving insights into mechanical and physical properties of a material.

### 1.2.3 Quantum dots

The production of QDs begin by enclosing electron gas into a two dimensional layer with thickness of some nm. A quantum wire further provides reduction to only one dimension freedom with quantum dots providing a zero dimensional lockup. In our report, one or two monolayers of InAs are brought epitactically onto a GaAs surface. The lattice mismatch of InAs on GaAs is about 7% causing 3 dimensional island of 2-4 nm in height a lateral extension of about 10-20 nm forming spontaneously.

### 1.2.4 Graphite

Graphite presents a hexagonal crystal system and is highly anisotropic. C atoms within each sheet is sigma bonded to three carbon atoms. The laminated structure is presented in Figure 10.

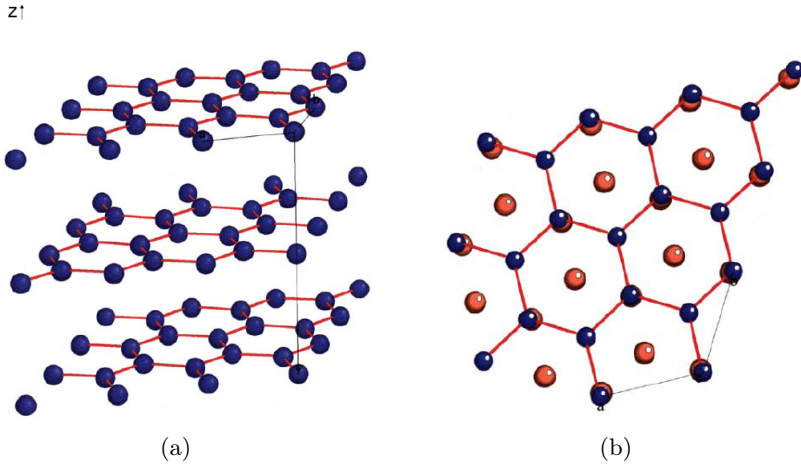


Figure 10: (a) Sheet structure of graphite with lattice constant  $c = 0.6711$  nm and (b) Top view onto layers of graphite with atoms of bottom layer marked in orange [7]

The sheet-like layers experience van-der-Waal forces which provides binding. From Figure 10(b) we notice that some C atoms (marked in blue) do not have adjacent neighbors in the layer below. This can be realized in the scanned images as neighbourless C atoms will appear brighter. As will be seen later in Figure 25(b), the STM image peaks correspond to stacked C atoms while the dark spots denote single C atoms. The difference in intensity occurs due to high tunneling current for stacked atoms.

### 1.2.5 Tantalum(IV) Sulfide

Similar to graphite,  $\text{TaS}_2$  is also a layered compound with three-coordinate sulfide centres and octahedral metal centres. It has three polymorphs presenting trigonal, hexagonal, and rhombohedral structures respectively [14].

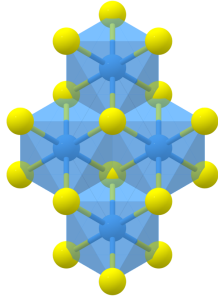


Figure 11: Trigonal polymorph of  $\text{TaS}_2$ . Data retrieved from the Materials Project for  $\text{TaS}_2$  (mp-1690) from database version v2023.11.1.

## 2 Experimental Setup

### 2.1 easyScan Operational Principle

The easyScan setup is presented below:

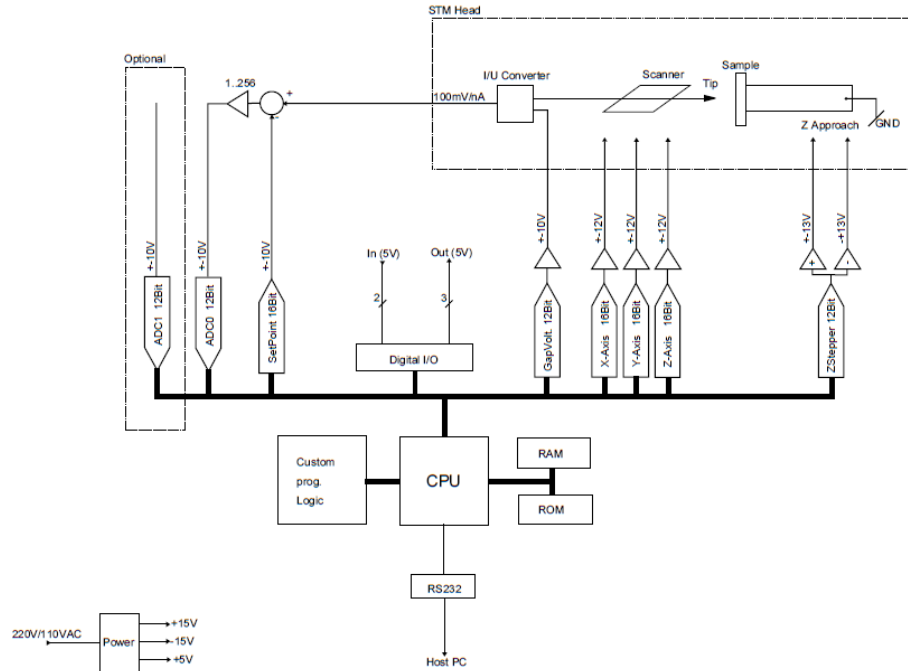


Figure 12: Schematic of easyScan setup with STM head, control electronics and host PC [7]

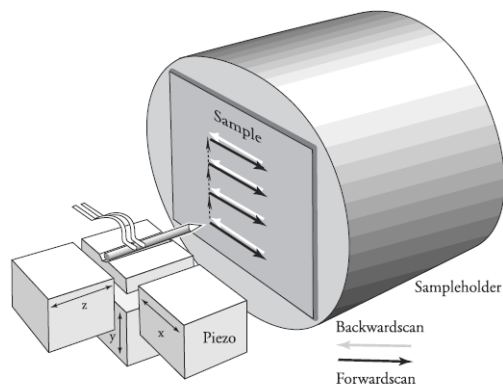


Figure 13: Microscope setup. The sample is located on a sample carrier (metal stem), which can be coarse moved with the help of a stepper motor. The  $x, y, z$  piezo motors move the tip across the specimen surface. [7]

The sample remains stationary while the tip scans the surface using three piezoelectric elements (x-, y-, and z-directions) with a maximum voltage of  $\pm 10$  V, enabling a scan range of 560 nm in x- and y-directions, and 200 nm in the z-direction. The sample is fixed to a metal stamp sample carrier held by a magnetic holder, which is moved by a stepper motor drive for coarse tip approach. The sample carrier is moved in a sawtooth pattern using another piezo crystal, enabling effective movement through friction. A tunnel voltage of -10 V to +10 V is applied between the tip and the sample, with the resulting tunnel current amplified and converted into a voltage by a trans-impedance converter, serving as the input for the z feedback control electronics.

## 2.2 Tip & Sample Handling

The scanning tip is prepared and installed by the supervisor.

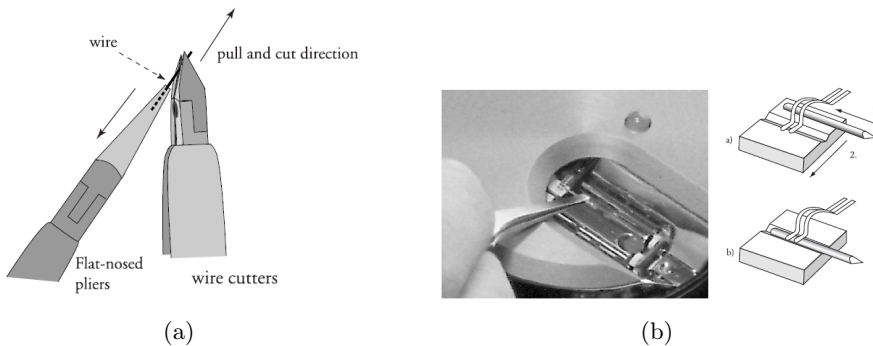


Figure 14: (a) Tip fabrication and (b) Tip installation [7]

The tip is made from a platinum-iridium wire, which is cut by twisting and pulling with a side cutter to produce a fine tip. Simple cutting is ineffective as it only compresses the wire.

Upon placement of sample onto the holder, the Naio software is used to manually coarse approach the sample surface as close to the tip as possible ( $\sim 1$  mm). This process is aided by a magnification lens on the microscope enclosure.

### 3 Results & Discussion

#### 3.1 Measurements of the Calibration Grid

In order to test the quality of our STM setup, we image a calibration grid (SN: 3206J0134). This consists of a Silicon layer with Aluminum bumps on it. The scan range was kept at 500 nm and we looked at the central area of the sample, where the periodic arrangement of the Aluminium bumps would be easily resolved. This as well as all other tasks, are almost entirely executed by mean of the software *Gwyddion* [8]. The resulting scans are the following:

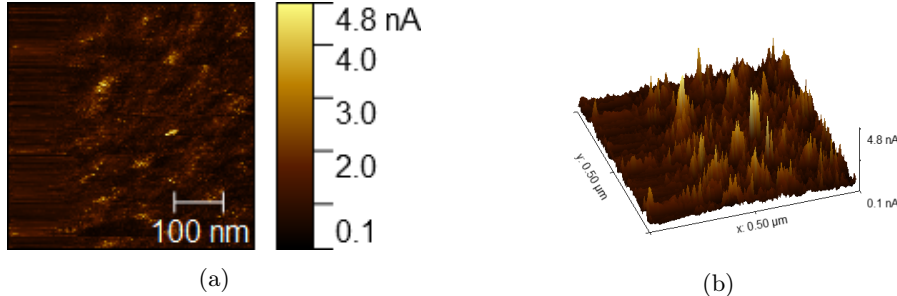


Figure 15: SN: 3206J0134 in Tip Current Forward mode: (a) 2D grid (b) 3D visualization.

In Tip Current Forward mode our results were not optimal - especially on the left side of the image, but the 3d visualization of the data (Fig. 15 (b)) allows us to observe hints of the periodic arrangement of the Aluminium atoms, represented by yellow peaks of the current. These peaks are aligned vertically and to that end, we choose an optimal x position ( $x=341$  nm, with (0,0) being the top left corner) and extract the vertical profile. Once we filter it to reduce noise, the following curve is observed:

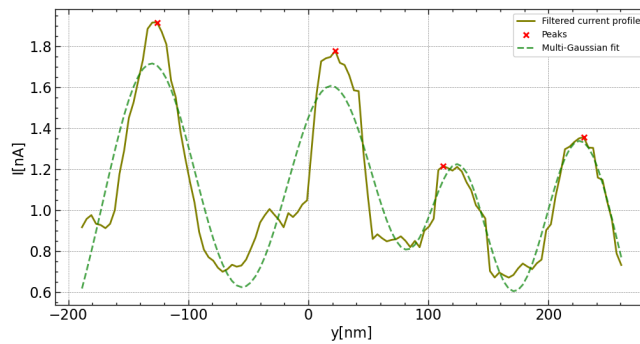


Figure 16: Visualization of the vertical profile of SN: 3206J0134 against the intensity of the current with peaks and Gaussian fit

One can extrapolate the vertical position of aluminium peaks by means of a fit (each peak is normally distributed). Subtraction of subsequent peaks positions

will give the average vertical distance between near neighbours peaks:

$$d = 118.89 \pm 15.56 \text{ nm} \quad (17)$$

We additionally looked at the Z-axis forward mode, which produced the following results:

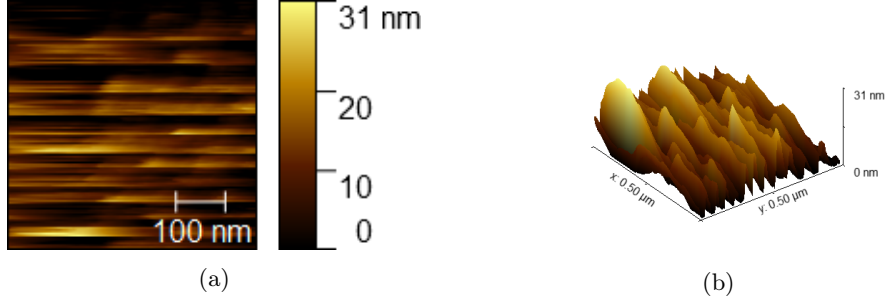


Figure 17: SN: 3206J0134 in Z-axis forward mode: (a) 2D grid (b) 3D visualization.

The mismatch between the lower and upper part of this scan hints to a substantial **thermal drift** in our measurements. If temperature variations are present, the image's lower part, which is scanned later with respect to the upper part, is stretched as thermal drifts are very clearly perceptible on an atomic scale. The cover reduces air flow around the scanner to avoid severe changes, but even variations of  $1/10^\circ\text{C}$  causes issues. The main source of thermal fluctuation is heating due to current.

Exact estimation of the thermal drift proved difficult due to the low quality of the data, but an attempt was made by the estimation of the peak to peak distance at different heights (fig. 17 (b) helps visualizing it).

We used 10 scans as data points, each of which allowed us to identify the average horizontal distance between two Aluminium atoms on that specific horizontal plane. The general behaviour we obtain is the following:

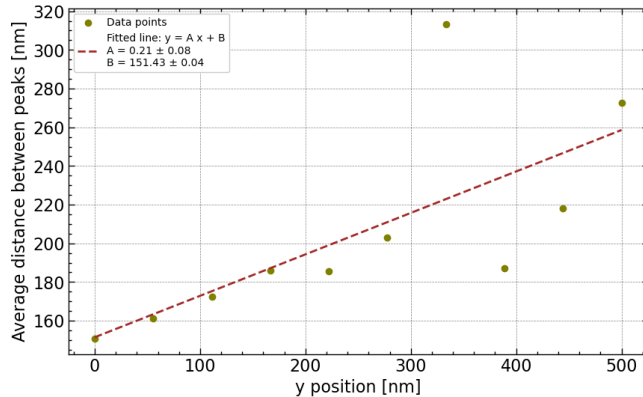


Figure 18: General behaviour of the average distance between peaks with respect to scan height  $y$

We see that the average peak distance increases almost linearly up till about 200 nm, in accordance to our expectation.

The intercept parameter  $B = 151.43 \pm 0.04$  nm gives us an extrapolated estimation (albeit not very accurate due to low density of points) of the inter-peak distance in absence of thermal drift, which is expected to be 160 nm according to [7]. The slope represents the positional increment coefficient. The setup employs 130 channels at a scanning speed of 1 channel/499 ms. Hence, for a 500 nm scan range, it yields a scanning velocity of 77 nm/s. That entails a thermal drift of  $16.17 \pm 6.16$  nm/s, which is significant when comparing with Si/Al lattice parameters of about 0.4-0.5 nm.

### 3.2 Gold (111) Sample

A measurement of a Gold sample was conducted with the aim of gaining information about its surface morphology with respect to the fabrication procedure. The tip voltage was increased to 400 mV with a Time/Line of 0.3 seconds, with the chosen range reduced to 300 nm. We observed creases towards the center of our golden sample, as such we made sure to image a region off-center.

The obtained scans in Z-axis forward mode were the following:

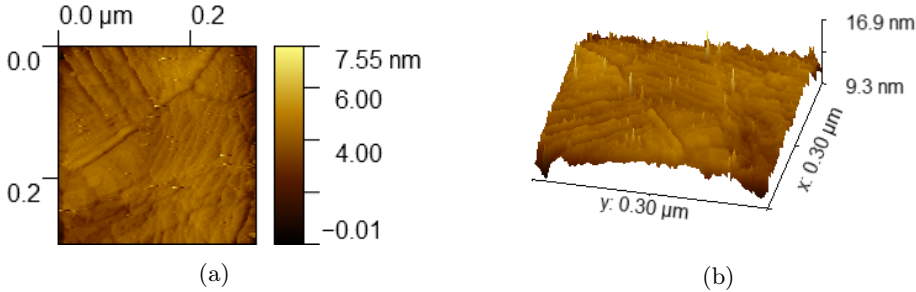


Figure 19: Gold sample in Z-axis forward mode: (a) 2D grid (b) 3D visualization.

Large mounts and valleys are observed, which seem to indicate an evolving film structure as discussed by M.J. Rost in [9]. Atoms experience an energy barrier when moving down a step edge on a surface. This causes atoms to accumulate at the step edges, rather than moving smoothly across the surface. This tendency to stick to the top of the edges rather than descending creates the mound like formations as seen in Figure 21(b). An analysis of the grains by segmentation allows us to observe the following:

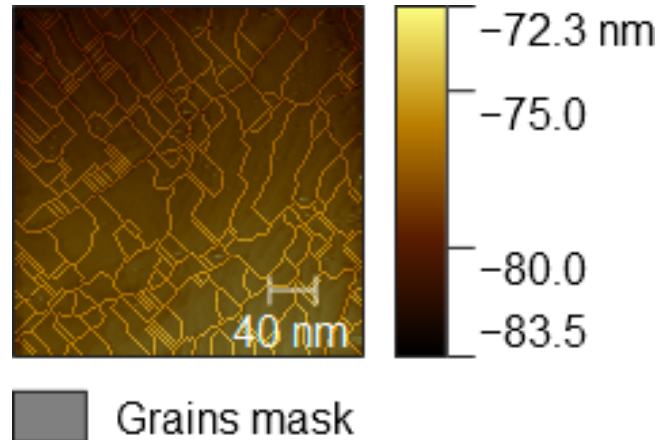


Figure 20: Visualization of grains on a gold (111) surface

With a 10 nm Gaussian smoothing, we identify a total of 394 grains, with a mean grain area of 193.39 nm<sup>2</sup>.

### 3.3 InAs Quantum Dots on a GaAs Surface

InAs quantum dots on a GaAs surface were measured. The chosen tip voltage was 50 mV and the scan range of 100 nm. The results of the scan in Z-axis forward mode are the following:

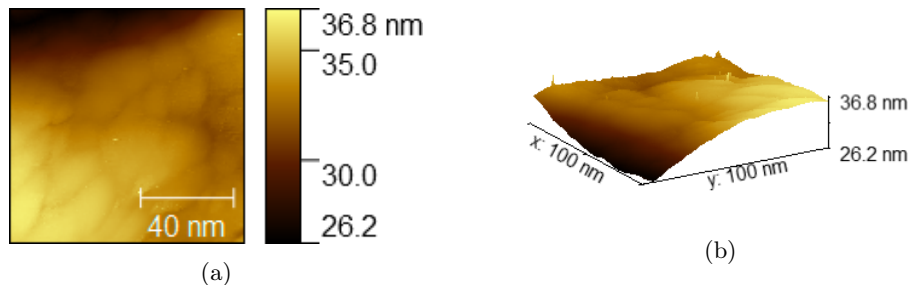


Figure 21: InAs quantum dots on a GaAs surface in Z-axis forward mode: (a) 2D grid (b) 3D visualization.

The general elongated shape in these grain like formations is quite evident. We analyze the formation of the dots by a grain selection by segmentation mode, which allows to identify 36 different grains of varying shape and size:

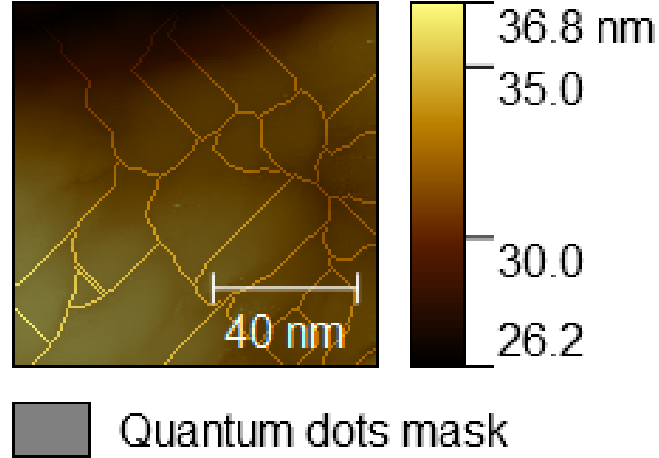


Figure 22: Visualization of InAs quantum dots on a GaAs surface

We can extract statistics regarding the dimension of each of the grain. This give the following distributions:

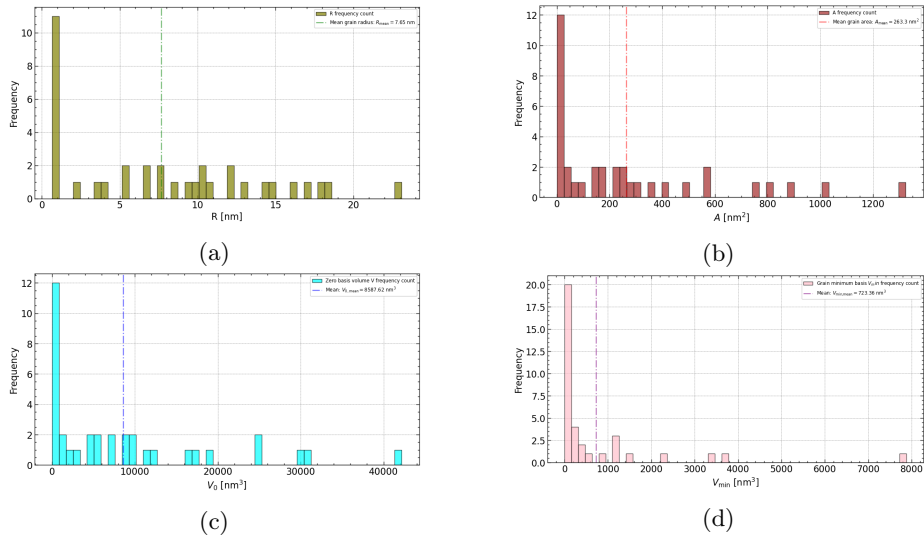


Figure 23: Histograms of quantum dots parameters distribution with respect to (a) grain radius, (b) grain area, (c) grain *zero basis* volume and (d) *grain minimum basis* volume.

According to section 1.2.3, a lateral extension of 10-20 nm is in line with the mean radius (Fig. 23 (a)), which gives a diameter of 15.3 nm. Of particular interest are the two different ways to estimate the quantum dots volume:

- **Zero basis:** the volume between grain surface and the plane  $z = 0$ .
- **Grain minimum basis:** the volume between grain surface and the plane  $z = z_{\min}$ , where  $z_{\min}$  is the minimum height occurring in the selected grain.

This method accounts for grain surrounding but it typically underestimates the volume, especially for small grains.

The second method (Fig. 23 (d)), as well as the mean Area (Fig. 23 (b)), gives us a best estimation for the mean height of the quantum dots:

$$h_{\text{mean}} = \frac{V_{\text{min,mean}}}{A_{\text{mean}}} = \frac{723.36 \text{ nm}^3}{263.3 \text{ nm}^2} = 2.75 \text{ nm}$$

### 3.4 Graphite Surface Morphology

We now examine the surface of a graphite sample (No. BT00628). A tip Voltage of 50 mV and a Time/Line of 0.06 was kept. We attempt to progressively decrease our scanning range ( $>100 \text{ nm}$ ), such that we may first identify an area seemingly devoid of defects, and then progressively zoom in until a 1 to 10 nm range is reached. Due to the reduced scan range, adjustment of PID-values is necessary, however, satisfactory image quality was not achieved:

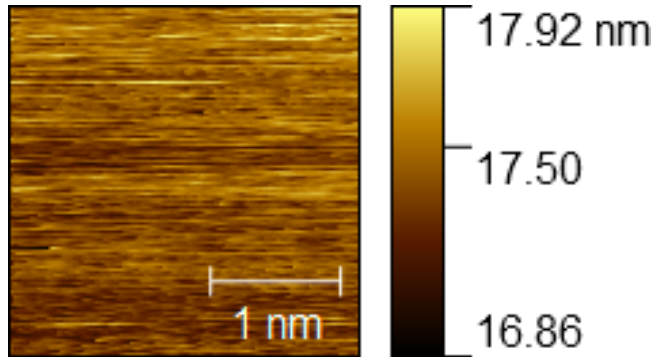


Figure 24: Example of an unresolved scan of Graphite in Z-axis forward mode. The PID-values were P-gain: 1800, I-gain: 800, D-gain: 0. The scan was attempted in a homogeneous region of sample.

The issue laid with the graphite tips, which either kept breaking or were not sharp enough to obtain good measurements. After multiple unsuccessful attempts, we were simply provided with the necessary data.

Using the Gwyddion software, we find the following scans for Graphite as seen in Figure 25.

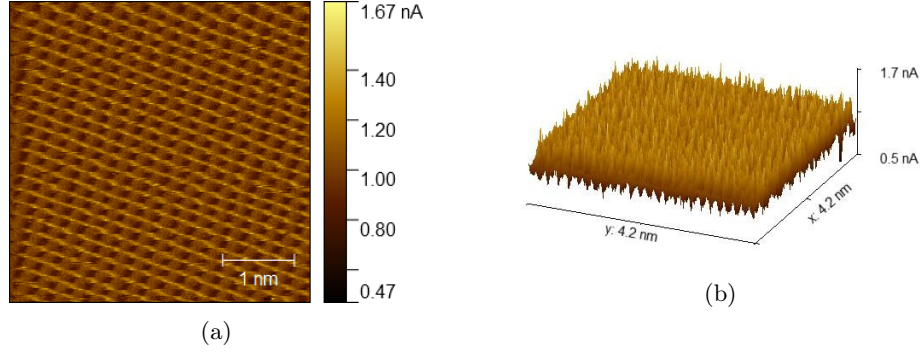


Figure 25: Graphite in Tip Current Forward mode: (a) 2D grid (b) 3D visualization.

Tip current forward mode (Fig. 25) particularly showcases the periodicity of the lattice, meanwhile in Z-axis forward mode (Fig. 26) one clearly notices the hexagonal structure of lattice.

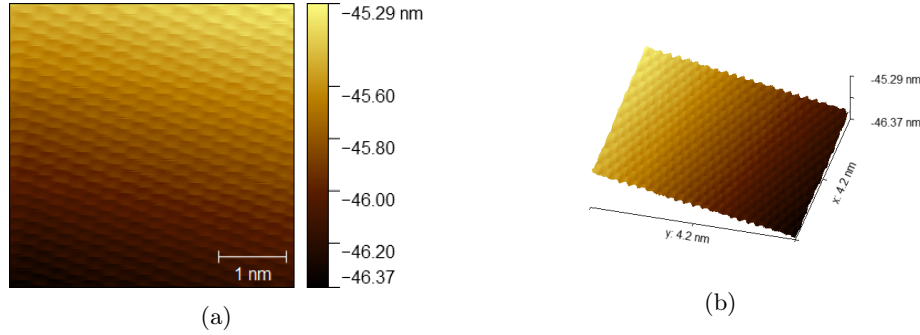


Figure 26: Graphite in Z-axis forward mode: (a) 2D grid (b) 3D visualization.

We then measure the lattice vectors using the *Data Process → Measure Features → Lattice* function on Fig. 25. After fitting it to our image, we obtain the following:

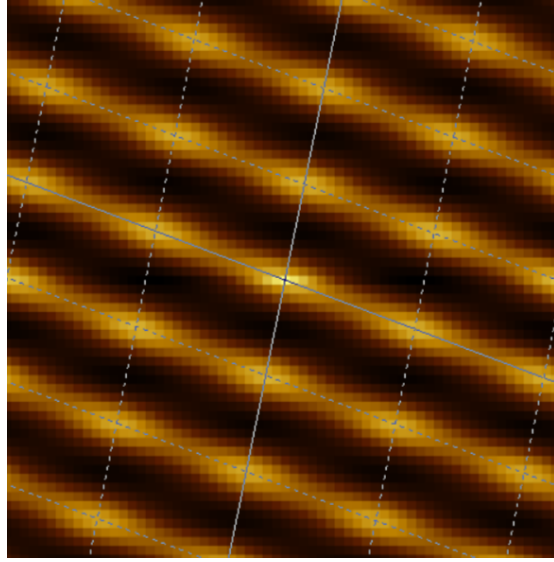


Figure 27: Lattice analysis of a graphite STM scan

This results in two lattice vectors  $\mathbf{a}_1$  and  $\mathbf{a}_2$  with a length and tilt  $\theta_i$  with respect to the horizontal axis of:

$$\begin{aligned} |\mathbf{a}_1| &= 0.250 \text{ nm}, \theta_1 = -20.39^\circ \\ |\mathbf{a}_2| &= 0.179 \text{ nm}, \theta_2 = 78.48^\circ \end{aligned}$$

A usual reference for lattice parameter of graphite is  $a = 0.246 \text{ nm}$  [16], which when compared to our  $a_1$  and  $a_2$  measurements present a deviation of 1.6% and 27.2% respectively. We derive the inter-atomic distance as  $a_{acc} = \frac{a}{\sqrt{3}}$ . For 2 different lengths of the lattice vectors, we find 2 inter-atomic distances:

$$\begin{aligned} a_{acc,1} &= 0.144 \text{ nm} \\ a_{acc,2} &= 0.103 \text{ nm} \end{aligned}$$

The angle between the lattice vectors is:

$$\Delta\theta = |\theta_1| + |\theta_2| = 98.87^\circ$$

which presents a significant error of 65% from the theoretical  $60^\circ$ . The hexagonal system of graphite can also be not observed from Figure 27. These deviations are likely due to thermal drift, the significant effects of which have been gauged in Section 3.1.

### 3.5 Charge Density Wave State of TaS<sub>2</sub>

As depicted in Section 1.2.5, TaS<sub>2</sub> forms a trigonal structure with octahedral Ta centres. Its polymorph 1T-TaS<sub>2</sub> undergoes first order charge density wave (CDW) phase transitions. CDW is a modulation of the electronic charge density in a material, accompanied by a periodic distortion of the atomic lattice. The electron gas forms a wave-like pattern with atomic displacement trying to lower the system's energy.

At low temperatures, this polymorph has a commensurate (i.e. the periodicity of CDW is a multiple of underlying crystal periodicity) CDW ground state. In this phase, the Ta atoms displace to make David Star clusters as shown in Figure 28.

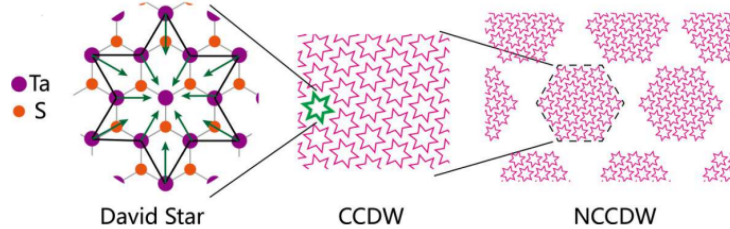


Figure 28: Schematic diagram of David Star and CCDW/NCCDW phases [17]

The outer 12 atoms move slightly towards the center of the star leading to the commensurate charge density wave (CCDW). At room temperature and ambient pressure we expect a nearly commensurate CDW state (NCCDW) with lattice parameter of  $a = 0.336$  nm for Ta-Ta distance in each triangular segment of the David Stars [18].

Analysis on a physical sample of  $\text{TaS}_2$  did not take place due to limitation of the experimental set up. The following segment centers around the analysis of Fig. 29 below, provided by the supervisor.

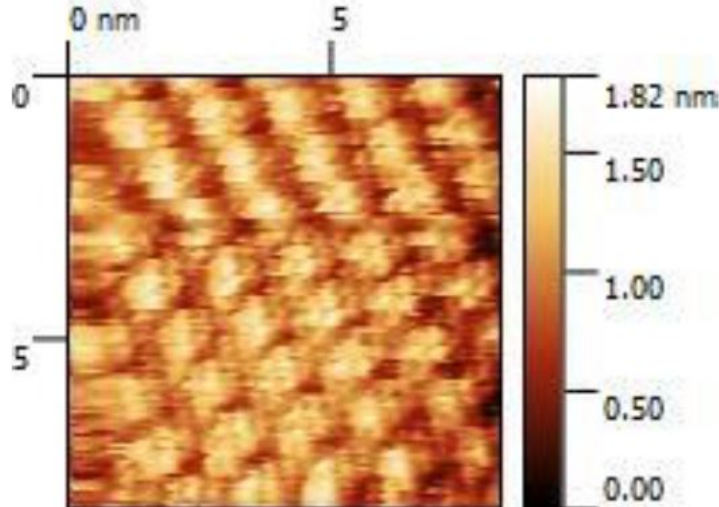


Figure 29: Provided STM scan of  $\text{TaS}_2$

Despite the low image quality, we extrapolate the scan range to be 8 nm (horizontally and vertically). This will result in the following:

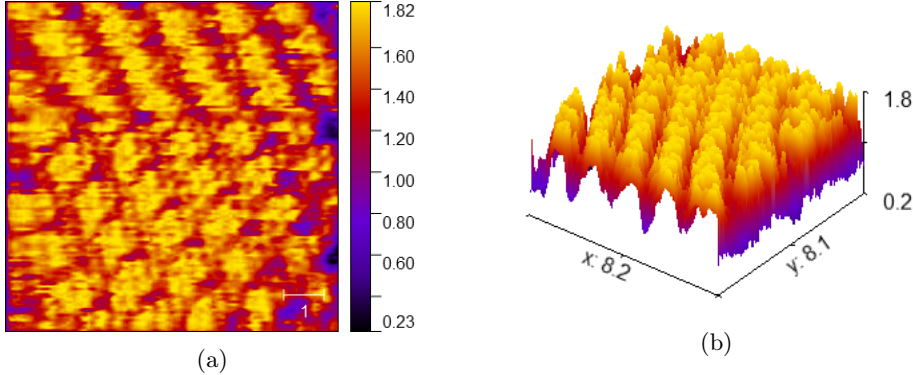


Figure 30:  $\text{TaS}_2$  in Z-axis forward mode: (a) 2D grid (b) 3D visualization. The unit of measure is nanometers

The exact vertex of the star-like formations are not resolved, but the periodicity of the cluster like arrangements can be noticed. Measurement of the lattice constants requires us to find the distance between nearby Tantalum atoms as depicted in Figure 28. This presents significant difficulties due to the clear presence of thermal drift, as well as the fact that Ta atoms themselves are not able to be singularly resolved within each cluster.

The Gwyddion function *Measure Lattice* under these conditions struggles to properly find a good estimation of a lattice constant. Additional functions, however, take the obtained data and transform them into a form that captures the regularity of the superlattice. The ACF (autocorrelation function image) and PSDF (Partial Scanning Density of States Function) are particularly well-suited for this because they exhibit peaks corresponding to the Bravais lattice vectors for the periodic pattern.

Peaks in the two-dimensional ACF correspond to lattice vectors in the direct space, while peaks in the two-dimensional PSDF correspond to lattice vectors of the reciprocal lattice. The matrices formed by the lattice vectors in direct and frequency space are transposed inverses of each other. With a suitable transformation either can be used to measure the lattice and are thus equivalent. This results in the following:

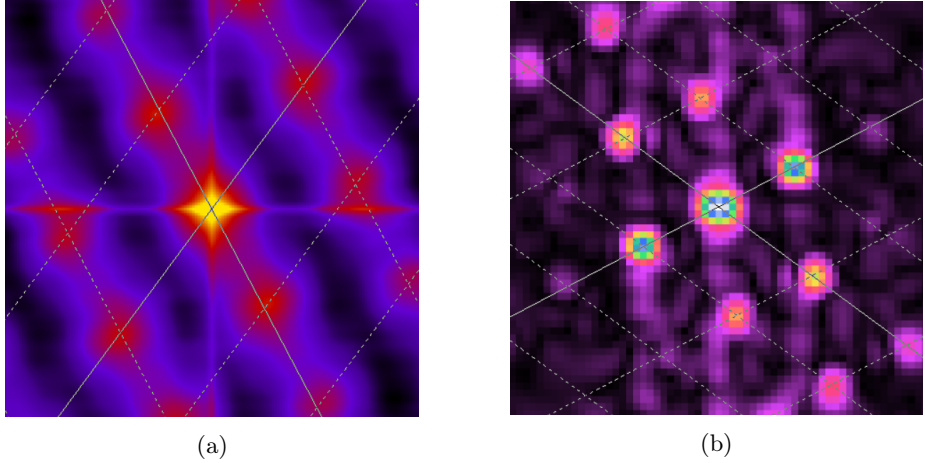


Figure 31:  $\text{TaS}_2$  lattice visualized in terms of (a) ACF and (b) PSDF

For the ACF image, we have intercluster distances  $A_1 = 1.076 \text{ nm}$ ,  $A_2 = 1.469 \text{ nm}$  with corresponding angles  $\phi_1 = -62.11^\circ$  and  $\phi_2 = 53.64^\circ$  with the horizontal respectively. This gives a total angle of  $\phi = 115.74^\circ$  between the two lattice vectors.

We have an average intercluster distance of  $\bar{A} = 1.272 \text{ nm}$  from which one can exploit the property of a commensurate state to extract an integer multiple of  $1.272/0.336 \approx 4$  with respect to the underlying lattice.

Additionally, an analysis of the clusters by grains segmentation was also performed, which allows us to isolate the different clusters with varying accuracy:

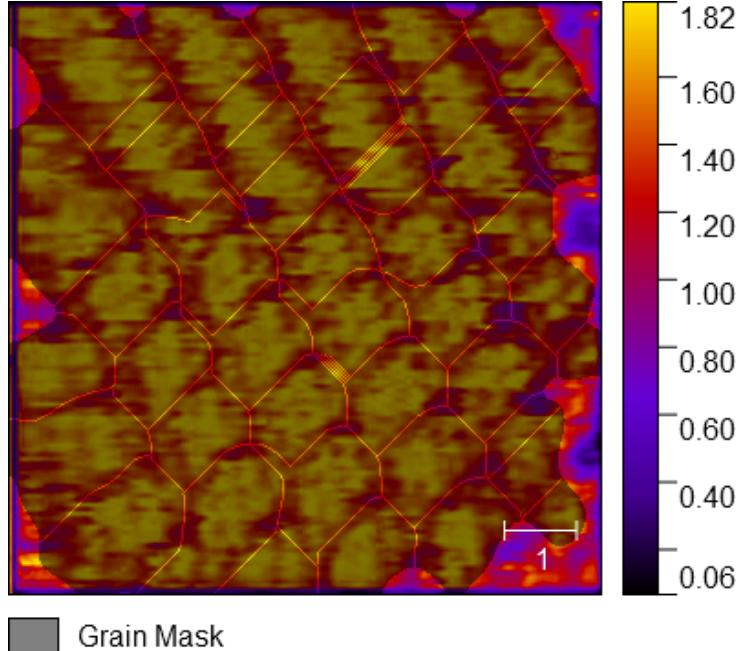


Figure 32: Grain analysis by segmentation of  $\text{TaS}_2$ . The unit of measure is nanometers

The corresponding mean cluster radius with respect to Fig. 32 was found to be  $0.263 \text{ nm}$  which presents a deviation of around 20% from literature value of Ta-Ta distance. This is due to imperfect tuning of the grain mask.

## 4 Conclusion & Outlook

After discussing the working principles of STM, a focus was made on investigating multiple samples. Even though STM is a powerful tool, it can create significant errors and it is imperative to understand why. The measurement of the calibration grid revealed an average bump distance of  $118.9 \pm 15.56 \text{ nm}$  along y-axis which hints at a significant thermal drift when compared to the expected  $160 \text{ nm}$ . However, a linear extrapolation to the beginning of the scan yielded  $151.43 \pm 0.04 \text{ nm}$  which is slightly better. We note that even though thermal effects might contribute to a slight systematic error in most experiments, at the atomic scale it can create significant deviations.

A large grain sample size of 394 was analyzed for (111) gold surface yielding an average grain area of  $193.39 \text{ nm}^2$ , along with expected mounds due to the Ehrlich-Schwoebel barrier. A similar grain segmentation analysis of InAs quantum dots on GaAs provided 36 segments with mean radius on par with expected lateral extensions.

For graphite, initial scans were unsuccessful due to issues with the tips, but provided data showed a periodic lattice structure with significant deviations likely due to thermal drift.

The clusters pertaining to a David Star superlattice in the commensurate state of  $\text{TaS}_2$  were observed and the lattice parameters extracted via different

methods. The clusters forming a 4-multiple of the underlying lattice was derived, with grain analysis of the clusters yielding Ta-Ta distance of 0.263 nm with 20% deviation from literature value.

Overall, while the STM provided insights into surface structures and morphology, the study highlighted the critical need for minimizing thermal drift and ensuring tip quality to enhance measurement accuracy.

## References

- [1] Binnig G, Rohrer H (1986). "Scanning tunneling microscopy". IBM Journal of Research and Development. 30 (4): 355–369. doi:10.1016/0039-6028(83)90716-1
- [2] B. D. Cullity; S. R. Stock. (2013). *Elements of X-Ray Diffraction, third edition*. Pearson
- [3] Escudero-Escribano, María. (2011). *Electrocatalysis and surface nanostructuring : atomic ensemble effects and non-covalent interactions*.
- [4] Rice, O. K. (1930). A contribution to the quantum mechanical theory of radioactivity and the dissociation by rotation of diatomic molecules. Physical Review, 35(12), 1538–1550. (URL:<https://doi.org/10.1103/physrev.35.1538>)
- [5] Zettili, N. (2022). Quantum Mechanics: Concepts and Applications. Wiley.
- [6] Scanning Tunnelling Microscopy/Scanning Tunnelling Spectroscopy (2009). Department of Physics. University of Warwick. (URL:<https://warwick.ac.uk/fac/sci/physics/current/postgraduate/regulations/pagswarwick/ex5/techniques/electronic/stm/>)
- [7] Riede V. Fritzsch W. Study of Solid State Surfaces using a Scanning Tunneling Microscope. Leipzig University.
- [8] David Nečas. Petr Klapetek. *Gwyddion: an open-source software for SPM data analysis*. Cent. Eur. J. Phys. 10(1) (2012) 181-188
- [9] M. J. Rost, *In Situ Real-Time Observation of Thin Film Deposition: Roughening, Zeno Effect, Grain Boundary Crossing Barrier, and Steering*, Physical Review Letters, 99, 266101 (2007)
- [10] W. Azzam, *Temperature-induced phase transition; Polymorphism in BP2 SAMs on Au(111)*, Central European Journal of Chemistry 7(4), pp. 884-899 (2009)
- [11] Roedel, J. and Li, J.-F. (2018). Lead-free piezoceramics: status and perspectives. MRS Bulletin 43: 576–580.
- [12] Nanosurf AG. Nanosurf NaioSTM: Operating Instructions v3.8R0. 2017.
- [13] STM (2023). Physikalisches Institut, RWTH Aachen. (URL:<https://institut2a.physik.rwth-aachen.de/de/teaching/praktikum/Anleitungen/IntroductionSTMen.pdf>)
- [14] Wilson, J.A.; Di Salvo, F.J.; Mahajan, S. (1975). "Charge-density waves and superlattices in the metallic layered transition metal dichalcogenides". Advances in Physics. 24 (2): 117–201. doi:10.1080/00018737500101391
- [15] R.E. Smallman, A.H.W. Ngan. *Modern Physical Metallurgy (Eighth Edition)*. 2014. Pages 415-442. ISBN 9780080982045,
- [16] Stefanescu (2020). Recent Developments in Understanding Nucleation and Crystallization of Spheroidal Graphite in Iron-Carbon-Silicon Alloys. Metals. 10. 221. 10.3390/met10020221.

- [17] Shao (2015). Manipulating charge-density-wave in 1T-TaS<sub>2</sub> by charge carrier doping: A first-principles investigation. Physical Review B. 94. 10.1103/PhysRevB.94.125126.
- [18] A. W. Tsen. et.al.(2015). Structure and Control of Charge Density Waves in Two-Dimensional 1T-TaS

## Appendix A Crystal Systems and their d-spacing

Cubic:

$$a = b = c, \quad \alpha = \beta = \gamma = 90^\circ$$

$$\frac{1}{d_{hkl}^2} = \frac{h^2 + k^2 + l^2}{a^2}$$

Tetragonal:

$$a = b \neq c, \quad \alpha = \beta = \gamma = 90^\circ$$

$$\frac{1}{d_{hkl}^2} = \frac{h^2 + k^2}{a^2} + \frac{l^2}{c^2}$$

Hexagonal:

$$a = b \neq c, \quad \alpha = \beta = 90^\circ, \quad \gamma = 120^\circ$$

$$\frac{1}{d_{hkl}^2} = \frac{4}{3} \left( \frac{h^2 + k^2 + hk}{a^2} \right) + \frac{l^2}{c^2}$$

Rhombohedral:

$$a = b = c, \quad \alpha = \beta = \gamma \neq 90^\circ$$

$$\frac{1}{d_{hkl}^2} = \frac{(h^2 + k^2 + l^2) \sin^2 \alpha + 2(hk + kl + hl) \cos^2 \alpha - \cos \alpha}{a^2(1 - 3 \cos^2 \alpha + 2 \cos^3 \alpha)}$$

Orthorhombic:

$$a \neq b \neq c, \quad \alpha = \beta = \gamma = 90^\circ$$

$$\frac{1}{d_{hkl}^2} = \frac{h^2}{a^2} + \frac{k^2}{b^2} + \frac{l^2}{c^2}$$

Monoclinic:

$$a \neq b \neq c, \quad \alpha = \gamma = 90^\circ, \quad \beta \neq 90^\circ$$

$$\frac{1}{d_{hkl}^2} = \frac{h^2}{a^2 \sin^2 \beta} + \frac{k^2}{b^2} + \frac{l^2}{c^2 \sin^2 \beta} - \frac{2hl \cos \beta}{ac \sin^2 \beta}$$

Triclinic:

$$a \neq b \neq c, \quad \alpha \neq \beta \neq \gamma \neq 90^\circ$$

$$\frac{1}{d_{hkl}^2} = \frac{1}{V^2} (S_{11}h^2 + S_{22}k^2 + S_{33}l^2 + 2S_{12}hk + 2S_{23}kl + 2S_{13}hl)$$

The coefficients for triclinic crystals are given by  $S_{11} = b^2 c^2 \sin^2 \alpha$ ,  $S_{22} = a^2 c^2 \sin^2 \beta$ ,  $S_{33} = a^2 b^2 \sin^2 \gamma$ ,  $S_{12} = abc^2(\cos \alpha \cos \beta - \cos \gamma)$ ,  $S_{23} = a^2 bc(\cos \beta \cos \gamma - \cos \alpha)$ , and  $S_{13} = ab^2 c(\cos \gamma \cos \alpha - \cos \beta)$ , with  $V$  being the volume of the unit cell [2].